

# Atomistic simulations of crystal-melt interfaces in a model binary alloy: Interfacial free energies, adsorption coefficients, and excess entropy

C. A. Becker,<sup>1,\*</sup> D. L. Olmsted,<sup>2</sup> M. Asta,<sup>3</sup> J. J. Hoyt,<sup>4</sup> and S. M. Foiles<sup>2</sup>

<sup>1</sup>*Metallurgy Division, National Institute of Standards and Technology, Gaithersburg, Maryland 20899, USA*

<sup>2</sup>*Sandia National Laboratories, Albuquerque, New Mexico 87185, USA*

<sup>3</sup>*Department of Chemical Engineering and Materials Science, University of California–Davis, Davis, California 95616, USA*

<sup>4</sup>*Department of Materials Science and Engineering, McMaster University, Hamilton, Ontario, Canada L8S 4L7*

(Received 23 October 2008; published 24 February 2009)

Monte Carlo and molecular-dynamics simulations are employed in a study of the equilibrium structural and thermodynamic properties of crystal-melt interfaces in a model binary alloy system described by Lennard-Jones interatomic interactions with zero size mismatch, a ratio of interaction strengths equal to 0.75, and interspecies interactions given by Lorentz-Berthelot mixing rules. This alloy system features a simple lens-type solid-liquid phase diagram at zero pressure, with nearly ideal solution thermodynamics in the solid and liquid solution phases. Equilibrium density profiles are computed for (100)-oriented crystal-melt interfaces and are used to derive the magnitudes of the relative adsorption coefficients ( $\Gamma_i^{(j)}$ ) at six temperatures along the solidus/liquidus boundary. The values for  $\Gamma_1^{(2)}$ , the relative adsorption of the lower melting-point species (1) with respect to the higher melting point species (2), are found to vary monotonically with temperature, with values that are positive and in the range of a few atomic percent per interface site. By contrast, values of  $\Gamma_2^{(1)}$  display a much more complex temperature dependence with a large peak in the magnitude of the relative adsorption more than ten times larger than those found for  $\Gamma_1^{(2)}$ . The capillary fluctuation method is used to compute the temperature dependence of the magnitudes and anisotropies of the crystal-melt interfacial free energy ( $\gamma$ ). At all temperatures we obtain the ordering  $\gamma_{100} > \gamma_{110} > \gamma_{111}$  for the high-symmetry (100), (110), and (111) interface orientations. The values of  $\gamma$  monotonically decrease with decreasing temperature (i.e., increasing concentration of the lower melting-point species). Using the calculated temperature-dependent values of  $\gamma$  and  $\Gamma_1^{(2)}$  in the Gibbs adsorption theorem, we estimate that roughly 25% of the temperature dependence of  $\gamma$  for the alloys can be attributed to interface adsorption, while the remaining contribution arises from the relative excess entropy  $S_{xs}^{(2)}$ .

DOI: [10.1103/PhysRevB.79.054109](https://doi.org/10.1103/PhysRevB.79.054109)

PACS number(s): 64.70.D-, 05.70.Np, 68.08.-p, 81.30.Fb

## I. INTRODUCTION

In the solidification of a crystal from the melt, the excess free energy of the solid-liquid interface ( $\gamma$ ) is known to play a critical role in determining transformation rates and associated growth morphologies.<sup>1–4</sup> In alloys the effects of solute concentration on the magnitude and crystalline anisotropy of  $\gamma$  can thus have important consequences for the formation of solidification microstructures. In elemental metals solute additions can lead to changes in  $\gamma$  anisotropy sufficiently large to alter preferred growth directions in dendritic solidification (e.g., Refs. 5 and 6), and can even induce faceting along one or more crystalline orientations (e.g., Refs. 7–9). Solute-induced changes in the magnitudes of  $\gamma$  also influence solidification microstructures through their effects on nucleation kinetics and the selection of primary stable or metastable phases.<sup>2</sup> While the composition dependence of  $\gamma$  is thus an important issue in alloy solidification, the underlying microscopic nature of the interactions between solute atoms and crystal-melt interfaces, which underlie such dependencies, remains incompletely understood.

Within Gibbs' thermodynamic formalism for a planar interface, variations in  $\gamma$  due to changes in temperature ( $T$ ) and solute chemical potential ( $\mu_1$ ) in a binary mixture can be expressed as follows (e.g., Ref. 10):

$$d\gamma = -S_{xs}^{(2)}dT - \Gamma_1^{(2)}d\mu_1, \quad (1)$$

where  $S_{xs}^{(2)}$  is the relative excess entropy and  $\Gamma_1^{(2)}$  is an adsorption coefficient, denoting the relative enrichment or depletion of species 1 at the interface if the excess of species 2 is zero, as defined below. Generally, for interfaces involving a crystalline phase, another term should be added to the right-hand side of Eq. (1) to account for interface stress (e.g., Ref. 11); in the present work this term gives rise to negligible changes to  $\gamma$ , as the solid density along coexistence is nearly constant, and we will thus neglect it in what follows. In a binary alloy changes in temperature and chemical potential are coupled by the requirement of two-phase (solid-liquid) equilibrium, which by the Gibbs phase rule leaves only one independent intensive variable at fixed pressure. Thus, changes in concentration and temperature are directly coupled, and for the remainder of this paper we will refer to solute-induced changes in  $\gamma$  interchangeably either as “composition dependencies” or “temperature dependencies.” Equation (1) provides a convenient conceptual framework for considering composition dependencies of  $\gamma$  in terms of two distinct contributions. The first is the relative excess entropy, which is typically considered to be a major contribution to the magnitude of  $\gamma$  in elemental metals (e.g., Refs. 12–14). The adsorption coefficient gives rise to a separate contribution, associated with changes in the solute chemical

potential, which includes both entropic and energetic (chemical) contributions to the free energies of the bulk phases. The magnitude of the excess adsorption coefficients for crystal-melt interfaces has been estimated in atomistic simulations previously for a few model binary systems,<sup>15–18</sup> in the most recent of these studies, Monte Carlo (MC) simulations for concentrated Lennard-Jones (LJ) mixtures<sup>16</sup> yield estimates which are on the order of a few percent per interface site. In order to compute the magnitude of the effects of interfacial adsorption on the composition dependence of  $\gamma$ , an integration of Eq. (1) is required, which in turn requires knowledge of the temperature dependence of  $\Gamma$ . The lack of such information in previous simulation studies has prevented estimates of the relative magnitudes of the adsorption versus excess-entropy contributions to the composition dependencies of  $\gamma$  in Eq. (1).

The present work extends our previous simulation studies where we reported a Monte Carlo based methodology<sup>16</sup> for computing relative adsorption coefficients at crystal-melt interfaces and calculated the composition dependence of the magnitude and anisotropy of  $\gamma$  for a model Lennard-Jones binary system<sup>6</sup> using the capillary fluctuation method (CFM).<sup>19–23</sup> Here we extend this earlier work by computing the composition dependence of the relative adsorption coefficient and combine this information with the computed values of  $\gamma$  to estimate the magnitude and temperature dependence of the relative excess entropy. Further, we use these estimates to elucidate the relative importance of the  $S_{xs}^{(2)}$  and  $\Gamma_1^{(2)}$  contributions to Eq. (1) in dictating the composition dependence of  $\gamma$ . The remainder of this paper is organized as follows. In Sec. II we define the model system and review its bulk thermodynamic properties and phase diagram. The method for calculating adsorption coefficients is then reviewed, and results are presented for the composition dependence of  $\Gamma$ . In the following section we discuss technical details and results for the calculation of concentration-dependent values of  $\gamma$  using the CFM. Finally, we present the analysis leading to estimates of  $S_{xs}^{(2)}$ . The work is summarized in Sec. VI. The Appendix contains a summary of analyses undertaken to determine the sensitivity of the CFM results to details of the method.

## II. MODEL SYSTEM AND ITS BULK THERMODYNAMIC PROPERTIES

The Lennard-Jones alloy model used in this work has been described previously, and the methods for calculating bulk thermodynamic properties and phase equilibrium are discussed thoroughly in Ref. 6. Here we review only the important details. The form of the interatomic potential  $\phi_{ij}(r)$  between species  $i$  and  $j$  is given as follows:

$$\phi_{ij}(r) = 4\epsilon_{ij} \left[ \left( \frac{\sigma_{ij}}{r} \right)^{12} - \left( \frac{\sigma_{ij}}{r} \right)^6 \right], \quad (2)$$

where  $\sigma_{ij}$  and  $\epsilon_{ij}$  measure atomic size and interaction strength, respectively. For the cross-species interactions we employ the Lorentz-Berthelot mixing rules:<sup>24</sup>

$$\epsilon_{12} = \sqrt{\epsilon_{11}\epsilon_{22}}, \quad (3)$$

$$\sigma_{12} = (\sigma_{11} + \sigma_{22})/2, \quad (4)$$

so that the interatomic potential for the mixture is defined by two parameters:  $\beta = \epsilon_{11}/\epsilon_{22}$  and  $\alpha = \sigma_{11}/\sigma_{22}$ . In the present work we focus on a system with zero size mismatch (i.e.,  $\alpha=1$ ), and a ratio of well depths given as  $\beta=0.75$ . As in Refs. 6 and 16, we have chosen to truncate the Lennard-Jones potentials employing the scheme introduced by Broughton and Gilmer<sup>11</sup> in their studies of the structure and thermodynamic properties of crystal-melt interfaces. The potential is thus given as

$$\phi(r) = \begin{cases} 4\epsilon \left[ \left( \frac{\sigma}{r} \right)^{12} - \left( \frac{\sigma}{r} \right)^6 \right] + C_1, & r \leq 2.3\sigma \\ C_2 \left( \frac{\sigma}{r} \right)^{12} + C_3 \left( \frac{\sigma}{r} \right)^6 + C_4 \left( \frac{r}{\sigma} \right)^2 + C_5, & 2.3\sigma < r < 2.5\sigma \\ 0, & 2.5\sigma \leq r, \end{cases} \quad (5)$$

where the constants are given by  $C_1=0.016132\epsilon$ ,  $C_2=3.1366 \times 10^3\epsilon$ ,  $C_3=-6.8069 \times 10^1\epsilon$ ,  $C_4=-0.083312\epsilon$ , and  $C_5=0.74689\epsilon$ .

The bulk free energies of solid and liquid solutions in this model alloy system were computed at zero pressure employing the Monte Carlo thermodynamic integration methodology described in Ref. 16. In this approach the composition dependence of the free energy ( $G$ ) at a fixed temperature is parametrized as follows:

$$G(x_2, T) = T[x_2 \ln x_2 + (1 - x_2) \ln(1 - x_2)] + A_0(1 - x_2) + A_1(1 - x_2)^2/2, \quad (6)$$

where  $x_2$  denotes the mole fraction of species 2. The temperature-dependent coefficients  $A_0$  and  $A_1$ , derived through Monte Carlo thermodynamic integration, are given for solid ( $s$ ) and liquid ( $l$ ) phases in Table I. This table also lists the solidus and liquidus phase-boundary compositions ( $x_2^s$  and  $x_2^l$ ) derived from the calculated free energies employing the common-tangent construction, along with the corresponding total atomic densities ( $\rho_{\text{tot}}^s$  and  $\rho_{\text{tot}}^l$ ) for these coexisting phases. Representative plots of the activities, mixing free energies and the solid-liquid composition-temperature phase diagram are given in Fig. 1. Note that since the melting point of species 2 is higher than that of species 1, the former preferentially partitions to the solid while the latter partitions to the liquid. This partitioning behavior will be discussed further in relation to the calculated density profiles below.

## III. DENSITY PROFILES AND ADSORPTION COEFFICIENTS

In a binary alloy the relative adsorption coefficient  $\Gamma_i^{(j)}$  can be defined as the excess amount of solute (species  $i$ ) per unit area, with a dividing surface chosen to give zero excess solvent (species  $j$ ), although the value of this quantity, as defined in Eqs. (7) and (8) below, is actually independent of the choice of interface location.<sup>10</sup> In concentrated alloys the definition of “solute” and “solvent” species is somewhat ambiguous, so that in what follows we will present results for

TABLE I. Solidus and liquidus compositions, nonideal chemical potential fitting coefficients, and densities for each of the temperatures which were examined for the alloy with  $\beta=0.75$  and  $\alpha=1.0$ . Units on temperature  $T$  are  $\epsilon_{22}/k_B$ .

$T$	$x_2^s$	$x_2^l$	$A_0^s$	$A_1^s$	$A_0^l$	$A_1^l$	$\rho_{\text{tot}}^s$	$\rho_{\text{tot}}^l$
0.472	0.075	0.046	2.29	-0.312	2.06	-0.315	0.947	0.825
0.479	0.151	0.094	2.29	-0.312	2.06	-0.317	0.947	0.824
0.5025	0.332	0.222	2.31	-0.322	2.06	-0.323	0.947	0.822
0.539	0.573	0.437	2.33	-0.341	2.07	-0.333	0.948	0.822
0.580	0.812	0.720	2.34	-0.356	2.07	-0.336	0.946	0.823
0.603	0.926	0.886	2.35	-0.363	2.07	-0.352	0.946	0.826

both  $\Gamma_1^{(2)}$  and  $\Gamma_2^{(1)}$ ; for the purpose of integrating Eq. (1) it will be shown to be much more convenient to use the former for the system under consideration. The adsorption of species 1 with respect to species 2,  $\Gamma_1^{(2)}$ , is defined formally as

$$\Gamma_1^{(2)} = \Gamma_1 - \left( \frac{\rho_1^l - \rho_1^s}{\rho_2^l - \rho_2^s} \right) \Gamma_2, \quad (7)$$

where  $\rho_i^\alpha$  is the bulk density of species  $i$  in phase  $\alpha$ , and  $\Gamma_i$  is the interfacial excess of species  $i$  for an arbitrary choice of dividing surface. Note that if the dividing surface is chosen to give  $\Gamma_2=0$ , then  $\Gamma_1=\Gamma_1^{(2)}$  is just the excess amount of

species 1 per unit area. An equivalent relation for  $\Gamma_2^{(1)}$  can be written as

$$\Gamma_2^{(1)} = \Gamma_2 - \left( \frac{\rho_2^l - \rho_2^s}{\rho_1^l - \rho_1^s} \right) \Gamma_1. \quad (8)$$

Analogous expressions can also be written for the relative excess entropy in Eq. (1).<sup>10</sup> To compute numerical values of  $\Gamma_2^{(1)}$  or  $\Gamma_1^{(2)}$  requires knowledge of the equilibrium density profiles. Section III A reviews the methods used to obtain these profiles from Monte Carlo simulations. Results are presented and discussed in Secs. III B and III C.

### A. Method

The calculations of density profiles and adsorption coefficients were performed using simulation cells containing co-existing solid and liquid regions separated by (100)-oriented crystal-melt interfaces. The simulation cells were created and equilibrated in the same manner as described in Ref. 16, although for the systems considered here it was found that it was not necessary to employ molecular dynamics simulations for the equilibration of the system pressure. Monte Carlo simulations were employed to equilibrate simulation cells containing 4312 atoms, set up initially as perfect fcc crystals containing  $7 \times 7$  unit cells in the direction parallel to the interface and 22 unit cells normal. The in-plane lattice constant was chosen as that of the strain-free crystal, and a periodic length normal to the interface was chosen to give a total density corresponding to roughly equal volume fractions of the equilibrium solid and liquid phases. After melting half of the system, employing Monte Carlo simulations that sampled displacement degrees of freedom for half of the atoms at a high temperature and fixed volume, the compositions in the solid and liquid regions of the cell were adjusted according to the values derived from the phase-diagram calculations (see above). Subsequently, the systems were equilibrated in a semi-grand-canonical (SGC) Monte Carlo simulation,<sup>25</sup> which samples displacement degrees of freedom, changes in the species type for a given atom (to sample compositional fluctuations), and fluctuations in the length of the simulation cell normal to the interface. The trial moves were accepted or rejected employing a standard Metropolis algorithm for a SGC ensemble with imposed temperature, chemical potential difference ( $\Delta\mu$ ) between species 1 and 2, zero stress normal to the interface, and fixed area. For a

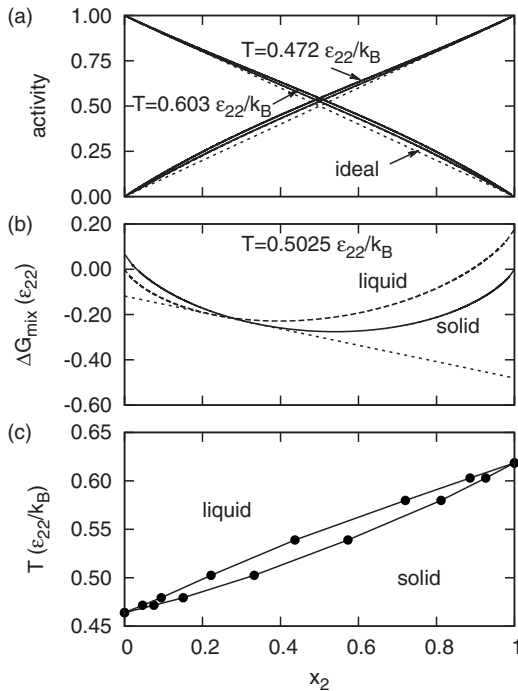


FIG. 1. (a) Activities as a function of composition for the solid and liquid phases for the alloy with  $\beta=0.75$  and  $\alpha=1.0$ . Solid and dashed lines correspond to solid and liquid phases, respectively, while the dotted line represents ideal-solution behavior. While both solid and liquid are plotted for  $T=0.472$  and  $0.603 \epsilon_{22}/k_B$ , they are so close in value as to not be readily distinguishable. (b) Mixing free energy with common tangent illustrated for  $T=0.5025 \epsilon_{22}/k_B$ . (c) Zero-pressure phase diagram calculated for this system.

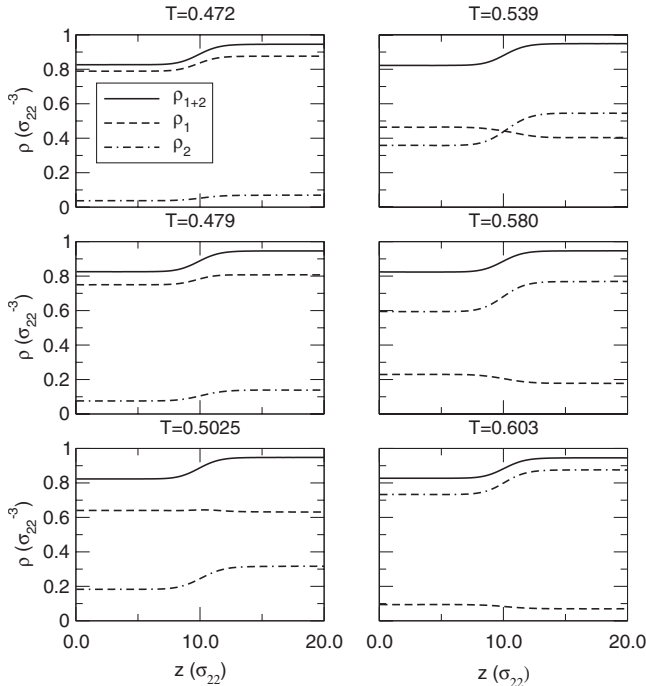


FIG. 2. Density profiles for each of the temperatures considered in this study. The solid line represents the total density, where the solid is located on the right and the liquid regions are shown on the left in each panel. The dashed line shows the density of species 1, while the dashed-dotted line is the density for species 2. Units on temperature  $T$  are  $\epsilon_{22}/k_B$ .

given temperature the values of  $\Delta\mu$  were chosen corresponding to two-phase equilibrium, as derived in the phase-diagram calculations described above.

Equilibration runs were performed for at least  $2 \times 10^6$  MC steps per atom, where a MC step consisted of a trial displacement, type change and/or change in periodic length. The equilibration of the system was assessed based on an analysis of system pressure, composition and energy, as described in Ref. 16. After equilibration, subsequent SGC-MC simulations were performed to generate a set of snapshots that were used to compute coarse-grained equilibrium composition profiles employing a finite-impulse-response (FIR) smoothing technique.<sup>26</sup> The details of the FIR analysis and the values of the filtering parameters employed in this work are the same as those described in Ref. 16. These simulations were performed considering 90 to 190 statistically independent subaverages, each of which consisted of runs lasting  $2.09 \times 10^5$  MC steps per atom. The density profiles and adsorption coefficients derived from each subaverage were averaged to yield the final results presented in Secs. III B and III C, and the variations between the results derived from each subaverage were used as the basis for estimating statistical uncertainties.

### B. Density profiles

Density profiles in the ( $z$ ) direction normal to the solid-liquid interface were calculated for a range of temperatures, as shown in Fig. 2. The solid lines represent the total atomic

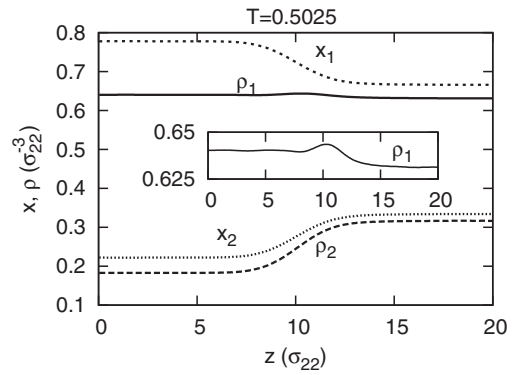


FIG. 3. Density ( $\rho_1$  and  $\rho_2$ ) and composition ( $x_1$  and  $x_2$ ) profiles at  $T=0.5025 \epsilon_{22}/k_B$ . A small density peak at the interface is visible in the profile for  $\rho_1$ .

density. In these plots the right-hand side corresponds to the solid region, while the liquid is on the left. The interface region can be clearly identified over the range of  $z$  showing finite density gradients. Note that the simulation cells are periodic in all dimensions with two solid-liquid interfaces along  $z$ , though only one of these two interfacial regions is plotted for clarity. The limiting (plateau) values of the density profiles in the solid and liquid regions correspond to the bulk values of the densities given in Table I. The total density in the solid is seen to be higher than that of the liquid at all temperatures.

The density profiles for the higher-melting-point species 2 are represented by the dashed-dotted lines in Fig. 2. As the temperature increases, the fraction of species 2 rises in the solid and liquid phases in accordance with the phase diagram. Consequently, the density curves for species 2 rise continuously with temperature;  $\rho_2$  is always higher in the solid than the liquid. There are two reasons for this. First, the total density is higher, and thus the volume-per-atom lower, in the solid than in the liquid. Second, species 2 partitions to the solid. These effects both contribute to making the density of species 2 higher in the solid than the liquid at all temperatures. The density profiles for species 1 are represented by the dashed lines in Fig. 2. It is seen that  $\rho_1$  is higher in the solid than the liquid at low temperatures, while the opposite is true at high temperatures. This effect is due to two competing factors. Again the total density is higher in the solid phase, which makes  $\rho_1$  higher in the solid at low temperatures where the mole fraction of species 1 ( $x_1 = 1 - x_2$ ) is large in both phases. However, as the temperature is raised from the lower melting temperature, element 1 increasingly partitions to the liquid. This has the effect of lowering the density of species 1 in the solid relative to the liquid, and at high temperatures this effect is strong enough to give a higher density of species 1 in the liquid rather than the solid. As a consequence of these competing effects, there is a temperature where the density of species 1 is equal in both the solid and liquid phases. The density profile for species 1 is thus extremely flat for  $T$  near this temperature, as illustrated by the results in Fig. 2 for  $T=0.5025$ , which is shown in more detail in Fig. 3. More apparent in Fig. 3 than in Fig. 2 is the presence of a small peak in  $\rho_1$  near the interface, which will be discussed further below.

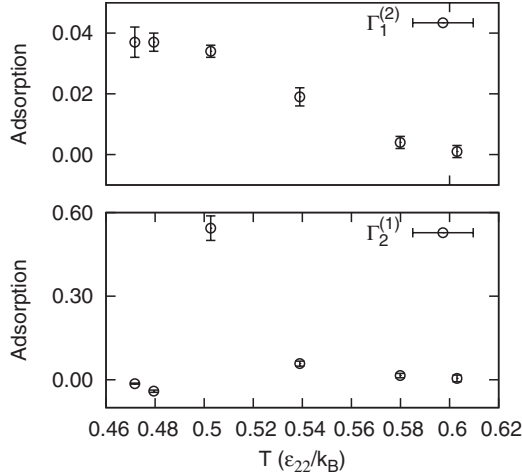


FIG. 4.  $\Gamma_1^{(2)}$  and  $\Gamma_2^{(1)}$  (atoms/site) versus temperature for  $\beta = 0.75$ ,  $\alpha = 1.0$ . Note the different scales of  $\Gamma_1^{(2)}$  and  $\Gamma_2^{(1)}$ . Error bars represent 95% confidence based on the adsorption subaverages as described in the text.

### C. Adsorption coefficients

Adsorption coefficients are calculated from the bulk (plateau) values of the filtered species densities for the solid and liquid phases in the simulation using formulations for  $\Gamma_1^{(2)}$  and  $\Gamma_2^{(1)}$  given by the following equations:<sup>15</sup>

$$\Gamma_1^{(2)} = \frac{1}{2A} \left\{ N_1 - \left( \frac{\rho_1^l - \rho_1^s}{\rho_2^l - \rho_2^s} \right) N_2 - AL_z \left[ \rho_1^s - \left( \frac{\rho_1^l - \rho_1^s}{\rho_2^l - \rho_2^s} \right) \rho_2^s \right] \right\} \quad (9)$$

and

$$\Gamma_2^{(1)} = \frac{1}{2A} \left\{ N_2 - \left( \frac{\rho_2^l - \rho_2^s}{\rho_1^l - \rho_1^s} \right) N_1 - AL_z \left[ \rho_2^s - \left( \frac{\rho_2^l - \rho_2^s}{\rho_1^l - \rho_1^s} \right) \rho_1^s \right] \right\}, \quad (10)$$

where  $A$  is the cross-sectional area of the simulation cell,  $N_i$  denotes the average number of atoms of species  $i$  in the SGC-MC simulation, and  $L_z$  is the length of the simulation cell normal to the interfaces. Equations (9) and (10) can be derived from Eqs. (7) and (8) assuming periodic boundary conditions, as described in Ref. 15. The bulk values of the densities required in the evaluation of Eqs. (9) and (10) are obtained by averaging the density values across the width of the plateaus of the FIR density profiles.

The relative adsorptions of species 1 and 2 versus temperature are shown in Fig. 4, and the values are given in Table II. We will begin by discussing the effect of temperature on  $\Gamma_1^{(2)}$ . The value of  $\Gamma_1^{(2)}$  is approximately 0.037 atoms/site for the lowest temperature,  $T = 0.472$ , closest to the melting point of species 1. With increasing temperature, and a corresponding decrease in the concentration of species 1 in the bulk phases, the calculated values of  $\Gamma_1^{(2)}$  decrease monotonically. All of the calculated values of  $\Gamma_1^{(2)}$  are found to be positive.

We consider next the calculated results for  $\Gamma_2^{(1)}$ . As the temperature is increased,  $\Gamma_2^{(1)}$  first becomes negative, reaching  $-0.041$  atoms/site, but then it becomes large and positive

TABLE II. Calculated adsorption coefficients for the LJ alloy systems considered. The units for  $\Gamma$  are atomic fraction per interface lattice site. Units on temperature  $T$  are  $\epsilon_{22}/k_B$ . The numbers in parentheses represent 95% confidence intervals associated with the last significant figure.

$T$	$\Gamma_1^{(2)}$	$\Gamma_2^{(1)}$
0.472	0.037(5)	-0.014(2)
0.479	0.037(3)	-0.041(4)
0.5025	0.034(2)	0.544(44)
0.539	0.019(3)	0.058(9)
0.580	0.004(2)	0.015(8)
0.603	0.001(2)	0.005(12)

with  $\Gamma_2^{(1)}$  increasing to a value of 0.544 at the temperature  $T = 0.5025$ . Further increases in temperature lead to a pronounced reduction in the magnitude of  $\Gamma_2^{(1)}$ . Positive values are found at higher temperatures with magnitudes on the order of a few percent per atomic site, comparable to the values found for  $\Gamma_1^{(2)}$ .

The most striking result of the adsorption calculations is the finding of a large peak in the magnitude of  $\Gamma_2^{(1)}$  over a relatively narrow temperature range. Though the peak is inherently mathematically possible in the definition of the Gibbs adsorption coefficients, it is important to consider the origin of this peak in further detail and to check that it is not an artifact of the analysis. The adsorption is calculated using Eq. (10) where the denominator contains a term representing the difference in densities of species 1 in the solid and liquid phases. At  $T = 0.5025$ , where we calculated the largest value of  $\Gamma_2^{(1)}$ , the difference  $\rho_1^l - \rho_1^s$  is very small with respect to  $\rho_2^l - \rho_2^s$  (see Fig. 3), leading to large contributions to  $\Gamma_2^{(1)}$  for  $T = 0.5025$ . Due to the way in which adsorptions are calculated using filtered density profiles in Eq. (10), it is desirable to check that the large magnitude of the adsorption coefficient is not an artifact arising from the use of the FIR procedure. We thus checked our values by computing  $\Gamma_2^{(1)}$  following three different numerical procedures.

First, instead of calculating the adsorption for each sub-average and then averaging those to find  $\Gamma_2^{(1)}$  and its standard error, we used Eq. (7) to calculate the adsorption from the average densities and then used propagation of errors to determine the standard error. Using this approach, we found  $\Gamma_2^{(1)} = 0.52 \pm 0.03$  atoms/site to 95% confidence. This check precluded large denominator fluctuations which could arise from abnormally small density differences. We also calculated the adsorptions using unfiltered profiles (as discussed in Ref. 16) and found  $\Gamma_2^{(1)} = 0.54 \pm 0.04$  atoms/site, in good agreement with the filtered profiles. Finally, we computed  $\Gamma_2^{(1)}$  directly from the averaged filtered density profiles using a Gibbs construction [rather than plateau values in Eq. (7)]. That is, we found the interface positions giving zero excess of species 1, i.e., where  $\Gamma_1 = 0$ . Then, the excess of species 2 was derived using this interface position, giving the value of  $\Gamma_2^{(1)}$  directly. In performing this calculation, it was found that the dividing surface was located not near the midpoint of the hyperbolic-tangent curve for the total density, but in the small density peak for species 1 on the solid side of the

interface. The shift of the dividing surface toward the solid leads to a relatively large value for  $\Gamma_2$ . This procedure gave rise to a value for  $\Gamma_2^{(1)}=0.52$  atoms/site, in excellent agreement with the other estimates at this temperature. We are thus confident that the large peak in  $\Gamma_2^{(1)}$  near temperatures of  $T=0.5025$  is a real effect and does not represent an artifact of the analysis. It is thus interesting to consider the form of  $\Gamma_2^{(1)}$  given in Eq. (8) in light of this result. Equation (8) implies that if one chooses an arbitrary dividing surface such that  $\Gamma_1$  and  $\Gamma_2$  remain finite at all temperatures, and if, as in the present case, the value of  $\rho_1^l - \rho_1^s$  changes from negative to positive, crossing through zero, with increasing  $T$ , and that both  $\rho_2^l - \rho_2^s$  and  $\Gamma_1$  are bounded away from zero, then  $\Gamma_2^{(1)}$  will necessarily diverge to negative  $\infty$  from below and positive  $\infty$  from above. Notice that this divergence of  $\Gamma_2^{(1)}$  does not imply any discontinuous physical behavior of the system, merely that there is a temperature where the concentration of species 1 is the same in both bulk phases.

Returning now to the original motivation for calculating the temperature dependence of the adsorption coefficient, we recall that our aim is to use these values in the integration of Eq. (1) to estimate the contributions of the relative excess entropy and interface adsorption to the composition dependence of  $\gamma$ . For this purpose, we are free to choose either species 2 or species 1 as the ‘‘solvent’’ for computing the relative adsorption coefficient, as discussed above. The results in Fig. 4 and the discussion above clearly indicate that the former is the preferred choice for performing such numerical integration, as  $\Gamma_1^{(2)}$  displays a relatively smooth and monotonic variation with temperature, while  $\Gamma_2^{(1)}$  displays strong and nonmonotonic variations over a narrow temperature range, which would present difficulties in the numerical integration of Eq. (1).

#### IV. INTERFACIAL FREE ENERGIES

In this section we discuss results for  $\gamma$  and its associated crystalline anisotropy calculated within the framework of the CFM.<sup>19–23</sup> While some of the main results in this section have been published previously,<sup>6</sup> we describe here the simulation and analysis methods in greater detail, and in the Appendix we summarize the findings of a number of tests aimed at assessing the magnitude of various systematic sources of error inherent in the CFM.

In the CFM, interfacial free energies and their associated crystalline anisotropies are derived from an analysis of equilibrium height fluctuations of the solid-liquid interface. The method is based on the following relation for fluctuations of sufficiently large wavelength [written here for a two-dimensional (2D) interface geometry, as used in the present work]:

$$\langle |A(k_1, k_2)|^2 \rangle = \frac{k_B T}{a(S_{11}k_1^2 + S_{22}k_2^2 + 2S_{12}k_1k_2)}, \quad (11)$$

where  $A(k_1, k_2)$  is the complex Fourier amplitude of the interface height profile,  $k_1$  and  $k_2$  denote the components of the wave vector along two orthogonal directions parallel to the interface,  $a$  is the cross-sectional area, and the brackets de-

note time (ensemble) averages. The  $S_{ij}$  are the components of the second rank stiffness tensor (e.g., Ref. 27), which is related to the interfacial free energy and its second derivatives with respect to interface orientation through the relation  $S_{ij} = \gamma \delta_{ij} + \partial^2 \gamma / \partial \theta_i \partial \theta_j$ . In the CFM the averages  $\langle |A(k_1, k_2)|^2 \rangle$  are derived from MD simulations and used to extract the interfacial stiffness components through Eq. (11). Values of the interfacial free energy are then derived from these calculated stiffnesses employing a symmetry-dictated expansion of  $\gamma(\hat{n})$  in terms of the components of the interface normal  $\hat{n} = (n_1, n_2, n_3)$  (Ref. 28):

$$\gamma(\hat{n})/\gamma_0 = 1 + \epsilon_1 \left( \sum_i n_i^4 - \frac{3}{5} \right) + \epsilon_2 \left( 3 \sum_i n_i^4 + 66n_1^2 n_2^2 n_3^2 - \frac{17}{7} \right), \quad (12)$$

where  $\gamma_0$  denotes the orientation-averaged interfacial free energy, and  $\epsilon_1$  and  $\epsilon_2$  are the magnitudes of the four and sixfold anisotropy terms. The approach described here has been used extensively in a number of previous calculations of  $\gamma$  (see, e.g., Refs. 20, 22, and 23 and references therein), although in most of this previous work ribbonlike, quasi-one-dimensional (1D) interface geometries were employed in the MD simulations, and a one-dimensional version of Eq. (11) was therefore used in the analysis. As discussed in Ref. 6, there are some advantages to using a 2D interface geometry in the CFM: only two simulations with (100) and (110) interface normals are necessary to derive three independent stiffness values (see below), compared to three different simulations required for the quasi-1D geometries. Also, more independent  $k$  modes are accessible in the 2D systems, since  $k$  vectors have the form [for a (100) interface with cross-sectional dimensions  $L \times L$  as a specific example]  $2\pi(j_x, j_y)/L$ , with either or both of the integers  $j_x$  and  $j_y$  nonzero.

#### A. Simulation details

The calculation of interfacial free energies based on the CFM requires simulation cells with relatively large cross-sectional areas in order to sample sufficiently long-wavelength modes. In the present work we have considered simulation cells with both (100)- and (110)-oriented crystal-melt interfaces. The dimensions of the periodic cells, along with the number of atoms and the total mole fraction of species 2 at each of the temperatures considered in this work are given in Table III. For reference, for the cells with (100)-oriented interfaces, the in-plane dimensions ( $L_x$  and  $L_y$ ) correspond to  $20 \times 20$  fcc unit cells, while the dimension normal to the interface corresponds to roughly 45 unit cells; comparable system sizes were used for the cells with (110)-oriented interfaces.

To equilibrate the different systems we first performed a combination of molecular-dynamics (MD) and MC simulations for the system at  $T=0.539$ , as described below. For all other temperatures the equilibrated systems at  $T=0.539$  were used to initialize the equilibration runs. Specifically, using an equilibrated simulation cell at  $T=0.539$ , a simulation cell for a different temperature was generated by scaling the periodic

TABLE III. Simulation details for the solid-liquid coexistence cells used in the capillary fluctuation studies. These include the temperatures ( $T$ ), interface orientations, cell dimensions, total number of atoms, and the total composition (roughly the average of the solidus and liquidus compositions). Units on cell dimensions  $L$  are  $\sigma_{22}$ . Units on temperature  $T$  are  $\epsilon_{22}/k_B$ .

$T$	Orientation	$L_x$	$L_y$	$L_z$	$N$	$x_2$
0.479	(100)	32.330	32.330	77.237	72000	0.120
0.479	(110)	34.291	32.330	80.209	79200	0.119
0.5025	(100)	32.310	32.310	77.737	72000	0.279
0.5025	(110)	34.269	32.310	80.799	79200	0.277
0.539	(100)	32.322	32.322	78.106	72000	0.509
0.539	(110)	34.281	32.320	81.188	79200	0.508
0.603	(100)	32.341	32.341	78.007	72000	0.906
0.603	(110)	34.308	32.346	81.338	79200	0.906
0.6185	(100)	32.340	32.340	76.587	72000	1.000
0.6185	(110)	34.308	32.346	80.169	79200	1.000

lengths and the composition in the solid and liquid regions in correspondence with the bulk densities and phase-boundary compositions at this new temperature.

The general procedure for equilibrating the simulation cells followed the method described in Ref. 16, and is similar to that discussed in Sec. III A. Starting from an initial state with roughly half solid and liquid, we alternated MC and MD runs to allow composition changes (MC) and global pressure relaxation (MD). The Monte Carlo runs were performed in the semi-grand canonical ensemble, as described in Sec. III A, to facilitate rapid relaxation of the composition profiles. The energy, pressure, and overall compositions were monitored during the simulations to determine when their values stabilized. These MC runs were often fairly short (approximately  $10^3$  or  $10^4$  MC steps per atom) since the initial compositions were set from the phase diagram calculation and were found to be very close to the values reached at equilibrium. The volume was constant in the MC runs, which sampled displacements with maximum magnitudes of about  $0.04\sigma_{22}$ , with approximately 55%–67% overall acceptance rates, and species type changes, with approximately 20%–50% acceptance rates. These initial MC runs were followed by MD simulations with NAP<sub>zz</sub>T or NVT ensembles to allow pressure relaxation through melting and crystallization. In the NAP<sub>zz</sub>T ensemble, only the dimension along  $z$  (normal to the interface) was allowed to fluctuate to accommodate volume changes from melting and solidification in order to maintain zero stress in that direction (i.e.,  $P_{zz}=0$ ), while the interfacial area  $A$  was held fixed to ensure a strain-free bulk crystal. The average temperature was maintained using a Nosé-Hoover thermostat and the pressure was regulated using a standard barostat.<sup>29</sup> We monitored the evolution of the pressure, volume, composition, and temperature in the MD simulations to check for equilibration. After an average of  $10^6$  steps in MD, the systems were moved back to MC for approximately  $10^4$  steps per atom to perform a final equilibration of the composition profiles. A subsequent final equilibration of approximately  $10^6$  steps per atom took place using NVT and NP<sub>zz</sub>AT MD simulations. All of the MD simulations used for equilibration and sampling made use of

LAMMPS (large-scale atomic/molecular massively parallel simulator).<sup>30</sup>

The final runs used to sample fluctuation amplitudes were performed in a microcanonical (NVE) ensemble for approximately  $2 \times 10^6$  MD steps for the alloys and the elemental (110) orientation. For the pure (100) system, the run length was approximately  $3 \times 10^5$  MD steps. The time step in the MD simulations was  $0.0002 (m\sigma_{22}^2/\epsilon_{22})^{1/2}$  in Lennard-Jones reduced units; this value of the time step was found to lead to good conservation of energy. Careful selection of an end point for the NAP<sub>zz</sub>T equilibration runs was found to be important to successfully transfer the simulations to the microcanonical ensemble employed in the sampling runs. If the final configuration is too far from the average (e.g., has a large pressure), the sampling runs may not be stable against melting or solidification. Snapshots were selected from the trajectories generated from these final sampling runs at a frequency of one per every  $10^3$  time steps, giving a total of 1556–40000 samples for use in the calculations of  $\langle |A(k_1, k_2)|^2 \rangle$  on the left-hand side of Eq. (11). Based on an analysis of correlation times, as described in Ref. 31, this sampling was found to yield estimates of  $\langle |A(k_1, k_2)|^2 \rangle$  converged to better than 2.4% in terms of estimated statistical uncertainties.

## B. Analysis and results

In this section we discuss the procedure used to analyze the results of the equilibrium fluctuation simulations described above. We describe the details of the methods used to identify interface locations and to fit the results, using Eq. (11), in the calculation of the concentration-dependent values of  $\gamma$  presented in Ref. 6. In the Appendix we discuss the sensitivity of these results to the details of the analysis procedures in order to estimate the magnitudes of various sources of systematic error.

Using symmetry, the form of Eq. (11) can be simplified for specific interface orientations. For a (100)-oriented interface, the fourfold and mirror-plane symmetries of the interface ensure that  $S_{11}=S_{22}=S$  and  $S_{12}=0$ . Thus Eq. (11) re-

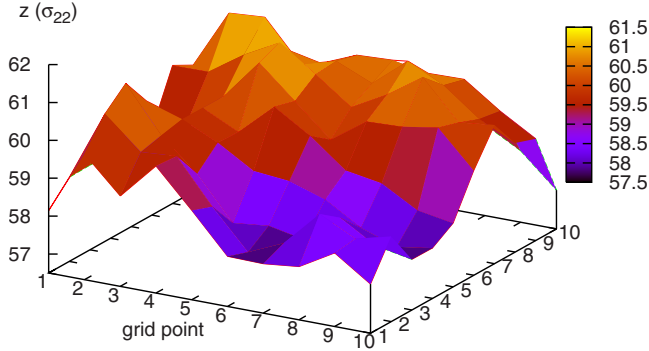


FIG. 5. (Color online) Sample interface height profile for an alloy with  $\beta=0.75$  and  $\alpha=1.0$ . The interface heights are determined for each column in a  $10 \times 10$  grid using a weighted mean value of the solid and liquid order parameters.

duces to the following simplified form which depends on only a single stiffness parameter, which we refer to simply as  $S$ :

$$\langle |A(k_1, k_2)|^2 \rangle = \frac{k_B T}{a S k^2}. \quad (13)$$

Similarly, for a (110) interface oriented with the  $x_1$  axis along  $[\bar{1}10]$  and the  $x_2$  axis along  $[001]$  the presence of a mirror plane and twofold symmetry implies that  $S_{11}$  is not equal to  $S_{22}$ , but  $S_{12}$  remains zero. In this case Eq. (11) reduces to the following form:

$$\langle |A(k_1, k_2)|^2 \rangle = \frac{k_B T}{a(S_{11}k_1^2 + S_{22}k_2^2)}. \quad (14)$$

The capillary fluctuation method requires identification of the interface location for each snapshot, and then application of Fourier transforms to compute  $A(k_1, k_2)$ , the squares of which are averaged to obtain estimates for the left-hand sides of Eqs. (13) and (14). For each interface, the instantaneous height profile was computed following the procedure analogous to that described in Ref. 19. A  $10 \times 10$  grid was formed parallel to the interface, and the value of the structural order parameter defined in Ref. 19 was computed and tracked normal to the interface in each of the  $10 \times 10$  columns, using a weighted averaging technique to obtain a smoothed order-parameter profile. A value of the order parameter well separated from those in the bulk solid and liquid phases, and roughly halfway between the average values in these phases, was used to identify the interface position in each column. A sample interface height profile generated by this procedure is shown in Fig. 5.

From the estimates of  $\langle |A(k_1, k_2)|^2 \rangle$  derived by time-averaging the Fourier intensities of the instantaneous height profiles, Eqs. (13) and (14) were used to derive the three independent stiffness values  $S$ ,  $S_{11}$  and  $S_{22}$  through a standard (unweighted) least-squares fitting procedure, considering data corresponding to all wave vectors  $k_{ij} = 2\pi(i/L_x, j/L_y)$  for which both  $i$  and  $j$  are less than 5. The sensitivity of the results to this cutoff was examined and the final value chosen as the one which gave the smallest statistical uncertainties in the stiffness values. The sensitivity of the results to the de-

TABLE IV. Stiffness values calculated at all temperatures considered in this work. Using the notation of Ref. 19,  $S$  is equivalent to the (100)[010] stiffness,  $S_{11}$  corresponds to a (110)[ $\bar{1}10$ ] stiffness, and  $S_{22}$  corresponds to (110)[001]. Units on stiffnesses are  $(\epsilon_{22}/\sigma_{22}^2)$ . Units on temperature  $T$  are  $\epsilon_{22}/k_B$ . Numbers in parentheses represent 95% confidence levels on the last digit.

$T$	$S$	$S_{11}$	$S_{22}$
0.479	0.225(7)	0.321(15)	0.220(8)
0.5025	0.267(7)	0.341(13)	0.249(8)
0.539	0.280(8)	0.380(17)	0.260(9)
0.603	0.295(8)	0.404(16)	0.300(10)
0.6185	0.286(6)	0.431(8)	0.305(9)

tails of the fitting procedure is described further in the Appendix. The resulting stiffness values for each of the orientations and temperatures considered in this work are given in Table IV and plotted in Fig. 6. Error bars on the calculated stiffnesses are  $2\sigma$  estimates of the statistical uncertainties, derived in a standard manner from the residuals of the least-squares fits. The stiffnesses are seen to generally increase with temperature. The value for the (100) orientation,  $S$ , is lower for the pure element than the alloy at  $T=0.603$ , although the error bars do overlap. The stiffness  $S_{11}$  is consistently higher than both  $S$  and  $S_{22}$ , which are similar in magnitude.

Interfacial free energies and their associated crystalline anisotropies were calculated from the fitted stiffness values using Eq. (12), as described previously (e.g., Refs. 21 and 31). In Table V, the orientationally averaged interfacial free energy ( $\gamma_0$ ) and anisotropy parameters ( $\epsilon_1$  and  $\epsilon_2$ ) derived from this analysis are listed. Also, the values of  $\gamma$  for the high-symmetry (100), (111), and (110) interfaces, derived from these values of  $\gamma_0$ ,  $\epsilon_1$ , and  $\epsilon_2$ , are presented for all temperatures studied. It is important to note that the values of  $\gamma$  for the pure elements obtained in this work agree to within the quoted statistical uncertainties with those calculated previously by the independent CFM (Ref. 22) and cleaving<sup>32–34</sup> methods.

The values of  $\epsilon_1$  and  $\epsilon_2$  in Table V are, respectively, positive and negative at all temperatures. The values of  $\epsilon_1$  are

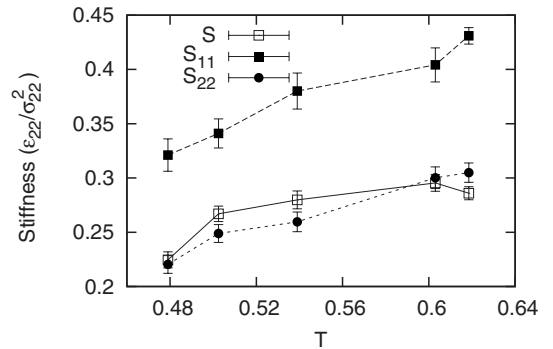


FIG. 6. Stiffnesses versus  $T$  for the (100) and (110) orientations. Error bars represent 95% confidence levels as described in the text. Units on temperature  $T$  are  $\epsilon_{22}/k_B$ .

TABLE V. Orientation-averaged interfacial free energies,  $\gamma_{100}$ ,  $\gamma_{110}$ ,  $\gamma_{111}$ , and anisotropy parameters for all temperatures studied. Units on  $\gamma$  are  $(\epsilon_{22}/\sigma_{22}^2)$ . Units on temperature  $T$  are  $\epsilon_{22}/k_B$ . The numbers in the parentheses represent estimates of the 95% confidence statistical uncertainties on the last digit.

$T$	$\gamma_0$	$\gamma_{100}$	$\gamma_{110}$	$\gamma_{111}$	$\epsilon_1$	$\epsilon_2$
0.464	0.267(6)	0.269(6)	0.265(6)	0.262(6)	0.057(6)	-0.0009(5)
0.479	0.270(8)	0.276(8)	0.270(8)	0.266(8)	0.055(7)	-0.0026(7)
0.5025	0.302(7)	0.307(7)	0.302(7)	0.298(7)	0.043(6)	-0.0033(6)
0.539	0.327(9)	0.333(9)	0.327(9)	0.321(9)	0.052(7)	-0.0037(6)
0.603	0.347(8)	0.353(8)	0.346(8)	0.342(8)	0.046(6)	-0.0015(6)
0.6185	0.355(8)	0.363(8)	0.354(8)	0.350(8)	0.057(6)	-0.0009(5)

seen to be roughly constant, while the values of  $\epsilon_2$  show a statistically significant trend toward larger magnitudes in the concentrated alloys. The implications of the anisotropy results have been discussed by us previously in the context of dendrite growth orientations.<sup>6</sup> The temperature dependence of the interfacial free energies is plotted in Fig. 7. Although the statistical uncertainties are relatively large, the results display the trend  $\gamma_{100} > \gamma_{110} > \gamma_{111}$  at all temperatures, consistent with previous calculated results for elemental fcc crystal-melt interfaces. It is apparent in Fig. 7 that the temperature dependence of the  $\gamma$  values is slightly nonlinear. In Sec. V we present an analysis of these calculated temperature dependencies in light of the results for interfacial adsorption given in Sec. III A; discussion of the sensitivity of the results to the details of the analysis is found in the Appendix.

### V. ADSORPTION AND EXCESS-ENTROPY CONTRIBUTIONS TO INTERFACIAL FREE ENERGIES

With the calculated results of  $\Gamma_1^{(2)}(T)$  and  $\gamma(T)$  for the (100) interface orientation, as well as the bulk calculated values of the chemical potentials, we are in a position to estimate the relative importance of the excess-entropy and interfacial adsorption contributions to Eq. (1) for dictating the temperature dependence of the crystal-melt interfacial free energy. By integrating Eq. (1) from the melting temperature of species 2 ( $T_M^{(2)}=0.6185$ ), to some lower temperature  $T$  (between  $T_M^{(1)}$  and  $T_M^{(2)}$ ) we obtain

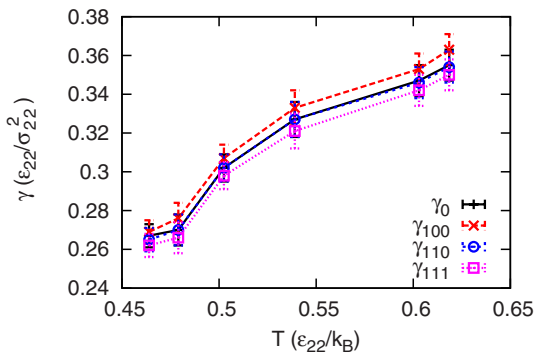


FIG. 7. (Color online) Interfacial free energy for each orientation, with the average orientation  $\gamma_0$  also shown. Error bars represent 95% confidence levels as described in the text.

$$\gamma_{100}(T) - \gamma_{100}(T_M^{(2)}) = I_1 + I_2, \quad (15)$$

where  $I_1$  is the contribution from the excess-entropy term on the right-hand side of Eq. (1):

$$I_1(T) = - \int_{T_M^{(2)}}^T S_{xs}^{(2)}(T') dT' \quad (16)$$

and  $I_2$  is the contribution from the adsorption term on the right-hand side of Eq. (1):

$$I_2(T) = - \int_{T_M^{(2)}}^T \Gamma_1^{(2)}(T') \frac{d\mu_1(T')}{dT'} dT'. \quad (17)$$

Since we have calculated the temperature dependence of  $\gamma_{100}$ ,  $\Gamma_1^{(2)}$  and  $\mu_1$ , we can compute  $I_2$  and use Eqs. (15) and (16) to derive an estimate for the magnitude of  $S_{xs}^{(2)}$ . The main difficulty with the analysis is finding a reliable way to model the temperature dependence for  $\Gamma_1^{(2)}$ ; while we calculated the values of  $\Gamma_1^{(2)}$  for a few discrete temperatures from Monte Carlo simulations, we need a denser sampling to be able to perform the integral in Eq. (17). Additionally, we need to ensure that we properly treat the singularity in  $d\mu_1/dT$  for  $x_1 \rightarrow 0$  (see below).

We will first consider the term  $d\mu_1/dT$  in Eq. (17). The Monte Carlo results show that the solution thermodynamics are close to ideal, so we can model the chemical potential as

$$\mu_1 = \mu_1^0(T) + k_B T \ln[x_1(T)], \quad (18)$$

where  $\mu_1^0(T)$  is the Gibbs free energy of pure species 1. Considering Eq. (18), we note that we can use either the liquid or solid values since, by coexistence, the two values are equal. To be explicit, we choose to consider the liquid, and  $d\mu_1/dT$  is then written as follows:

$$\frac{d\mu_1}{dT} = \frac{d\mu_1^0(T)}{dT} + k_B \ln[x_1(T)] + \frac{k_B T}{x_1(T)} \frac{dx_1}{dT}, \quad (19)$$

where  $x_1(T)$  is the mole fraction of species 1 on the liquidus boundary for a given temperature  $T$ .

In applying Eq. (19), we made use of a quadratic fit of the liquidus boundary  $x_1$  as a function of  $T$ . We also need to compute  $d\mu_1^0/dT$  from the thermodynamic-integration fits described above (since this is the derivative of the Gibbs free energy for pure species 1 in the liquid phase). Since  $dx_1/dT$  is finite approaching  $T_M^{(2)}$  (i.e., as  $x_1 \rightarrow 0$ ), the last term on the

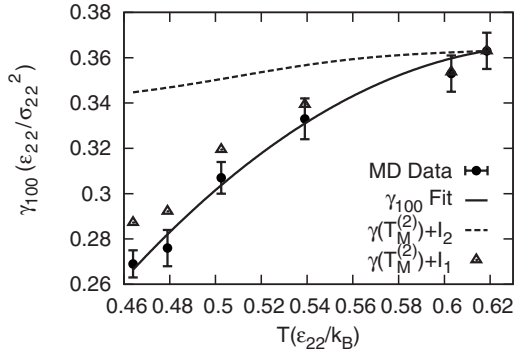


FIG. 8. Relative contributions to the interfacial free energy from the adsorption and relative excess entropy. Error bars on the interfacial free energies calculated from MD data represent 95% confidence levels as described in the text.

right-hand side of Eq. (19) blows up in this limit. Fortunately,  $\Gamma_1^{(2)}$  also goes to zero in this limit, and the product  $\Gamma_1^{(2)}(d\mu_1/dT)$  can be expected to be everywhere finite (see below).

We next derive a spline fit to represent  $\Gamma_1^{(2)}$  as a function of  $T$ . It is reasonable to assume that in the limit of  $x_1 \rightarrow 0$  the adsorption  $\Gamma_1^{(2)}$  should be linearly proportional to  $x_1$ ; such a dependence follows naturally in various mean-field expressions for solute adsorption (e.g., Ref. 35). In performing the spline fit we thus enforced that  $\Gamma_1^{(2)}$  is zero at  $x_1=0$ , and that the derivative of  $\Gamma_1^{(2)}$  with respect to  $x_1$  is finite in this limit. Once we have the spline fit for  $\Gamma_1^{(2)}$  versus  $x_1$ , we can substitute the fit for  $x_1$  versus  $T$ , generating a new expression for  $\Gamma_1^{(2)}$  versus  $T$ . This expression, plus Eq. (19) can then be used to numerically integrate Eq. (17). The result is the estimate for the contribution of  $I_2(T)$ . The resulting estimate is plotted as  $\gamma(T_M^{(2)})+I_2(T)$  by the dashed line in Fig. 8. It is readily seen that the adsorption contributions to Eq. (1) give rise to a decrease in  $\gamma$  with decreasing  $T$  which is relatively small in magnitude, on the scale of the overall 25% variation in  $\gamma_{100}$  over the relevant temperature range.

With the values of  $I_2(T)$  at the values of  $T$  for which  $\gamma_{100}$  was calculated, we can compute the magnitude of  $I_1(T)$  at each of the five temperatures below  $T_M^{(2)}$ . The results are plotted as the sum  $\gamma(T_M^{(2)})+I_2(T)$  by the open triangles in Fig. 8. The resulting values of  $I_2(T)$  are clearly seen to be much larger than those for  $I_1(T)$ . Finally, to estimate values for  $S_{xs}^{(2)}(T)$  we can perform a fit of the values of  $I_2$  versus  $T$  and from the resulting fit take the derivative  $dI_2(T)/dT = -S_{xs}^{(2)}(T)$  to derive values of the relative excess entropy. With the limited data available, the most robust results that could be obtained were for a linear fit of  $I_2$  versus  $T$ . The fit leads to the prediction of a constant value of  $S_{xs}^{(2)} = -0.45\sigma_{22}^{-2}$  for the (100) interface orientation.

An independent estimate of  $S_{xs}^{(2)}$  was also derived using the relation [from Eq. (1)]

$$\frac{d\gamma}{dT} = -S_{xs}^{(2)} - \Gamma_1^{(2)} \frac{d\mu_1}{dT}, \quad (20)$$

with the left-hand side evaluated using three-point Lagrange interpolation formulas for each of the alloy compositions

considered in the calculations of  $\gamma$  and  $\Gamma_1^{(2)}$ . The resulting values for  $S_{xs}^{(2)}$  contained large statistical uncertainties and hence no clear trend related to the composition dependence of the excess entropy could be derived. The averaged value for all compositions was  $S_{xs}^{(2)} = -0.6\sigma_{22}^{-2}$  (with standard deviation of 0.2). The analysis was also used to check the accuracy of the ideal solution approximation by using the activity coefficients derived from Eq. (6) in the evaluation of  $d\mu_1/dT$  in Eq. (20); the nonideal contributions were found to lead to less than 10% changes in the calculated values of  $S_{xs}^{(2)}$ .

Overall, the analyses described in this section give rise to estimates for the composition-averaged value of  $S_{xs}^{(2)}$  for the alloys ranging between  $-0.45$  and  $-0.6\sigma_{22}^{-2}$ . It is interesting to compare this estimate with previously published estimates for the excess entropy in pure elements. In 1983 Broughton and Gilmer<sup>36</sup> published calculated values of the excess energy  $E_{xs}$  in addition to interfacial free energies for crystal-melt interfaces in the Lennard-Jones system. From the difference in these values they derived an estimate of the excess entropy of  $S_{xs} = -0.08 \pm 0.15\sigma_{22}^{-2}$  where the large uncertainties were associated with difficulties in positioning the dividing surface in the calculation of  $E_{xs}$ . Further work is required to determine the source of the discrepancy between the current estimates and those of Broughton and Gilmer; two possibilities worth investigating would be intrinsic composition dependencies associated with the present results for alloys, or the use of relatively small system sizes in the early MD studies. The Broughton-Gilmer estimate, when multiplied by the melting temperature, accounts for only about 15% of the interfacial free energy of the Lennard-Jones system. We note that the larger estimates for  $S_{xs}^{(2)}$  obtained in the present work are qualitatively consistent with the theoretical model of Spaepen<sup>12</sup> which assumes that the crystal-melt interfacial free energy is purely entropic in origin. In the Spaepen model the large and negative values of  $S_{xs}$  arise from the reduction in hard-sphere packing entropy induced by the ordering of the liquid against the solid. In light of this interpretation, it is interesting to consider the density-functional theory results for  $\gamma$  in the Lennard-Jones system due to Curtin.<sup>37</sup> In his analysis, Curtin used a perturbation theory approach to estimate the hard-sphere contributions to  $\gamma$ , along with the contributions arising from the attractive part of the potential. The former, which are entirely entropic in nature, were found to constitute between 85 and 90% of the total magnitude of  $\gamma$ . The large value of the hard-sphere entropic contribution to  $\gamma$  is again consistent with the larger values for  $S_{xs}^{(2)}$  derived in the present work.

## VI. SUMMARY AND CONCLUSIONS

In this work atomistic simulations have been employed in a study of the equilibrium structural and thermodynamic properties of crystal-melt interfaces in a model Lennard-Jones binary alloy system characterized by zero atomic size-mismatch ( $\alpha=1$ ) and a ratio of well depths of  $\beta=0.75$ . This system features nearly ideal solution thermodynamic properties and a simple phase diagram with disordered solid and liquid solution phases connected by a simple lens-shaped solid-liquid two-phase region. The results of our calculations

for the phase diagram and bulk solution-thermodynamic properties are consistent with earlier studies.<sup>16,38</sup>

We have considered crystal-melt interfaces for six different temperatures along the solidus/liquidus boundary and have calculated coarse-grained density profiles for (100)-oriented interfaces in each system. The total densities and the density of the higher melting-point species (2) display profiles at each temperature characterized by roughly hyperbolic-tangent shapes with higher densities in the solid phase. For the lower melting-point species (1) the density is higher in solid than liquid at low temperatures, while the opposite is found at high temperatures. A temperature thus exists where the profile of  $\rho_1$  is equal in the solid and liquid phases, and near this temperature the density profile is extremely flat and is found to display a small peak near the interface. This behavior has important consequences for the magnitudes of the relative adsorption coefficients derived from these profiles. While  $\Gamma_1^{(2)}$  is found to display a smooth temperature dependence, rising from zero to a maximum value of approximately 0.04 atoms per interface site as the temperature is decreased from  $T_M^{(2)}$  to  $T_M^{(1)}$ , the behavior of  $\Gamma_2^{(1)}$  is much more complex. As the temperature is raised from  $T_M^{(1)}$ ,  $\Gamma_2^{(1)}$  starts out negative with a magnitude similar to those found for  $\Gamma_1^{(2)}$ ; with further increases in temperature, a large and positive value is obtained which decays to much lower values as  $T_M^{(2)}$  is approached. The complex behavior of  $\Gamma_2^{(1)}$  is attributed to the behavior of the density profiles of species 1 over the range of temperatures where  $\rho_1$  is nearly equal in the bulk solid and liquid phases.

The method surrounding the calculations of the magnitudes and anisotropies of the crystal-melt interfacial free energy ( $\gamma$ ), as reported by us previously,<sup>6</sup> has been described in detail. The interfacial free energies are found to have magnitudes that decrease monotonically as the temperature is decreased from  $T_M^{(2)}$  to  $T_M^{(1)}$ . At all temperatures we obtain the ordering  $\gamma_{100} > \gamma_{110} > \gamma_{111}$  for the high-symmetry (100), (110), and (111) orientations. The magnitudes of the  $\gamma$  anisotropies display composition dependencies that are significant on the scale required to induce morphological transitions in dendrite growth.<sup>6</sup> For the present system these composition dependencies are characterized by a nearly constant value of the fourfold anisotropy coefficient ( $\epsilon_1$ ), with sixfold ( $\epsilon_2$ ) coefficients that are negative and increase in magnitude as the solute concentration is increased starting from both of the pure elements.

In a recent study by Amini and Laird,<sup>39</sup> composition-dependent values of  $\gamma$  and associated crystalline anisotropies were derived from the capillary fluctuation method for a hard-sphere mixture with a size ratio of 0.9. The results display a temperature dependence of  $\gamma_0$  (at fixed pressure) qualitatively similar to ours, and the ordering of  $\gamma$  values for (100), (110), and (111) interfaces is also consistent with the present calculations. Interestingly, however, Amini and Laird find that  $\epsilon_1$  increases considerably in magnitude with increasing concentration of the higher melting point species, while  $\epsilon_2$  remained roughly constant. The results are qualitatively different from those found here for a system with no size mismatch, and Amini and Laird speculate, based on this comparison, that size and chemical effects may play distinct roles in determining the composition dependence of  $\gamma$  aniso-

tropy in alloys. Further work for a wider range of systems would clearly be helpful to explore these effects in greater detail.

The calculated temperature-dependent values of  $\gamma$  and  $\Gamma_1^{(2)}$  were employed in an analysis based on the Gibbs adsorption theorem to estimate the relative importance of adsorption and excess-entropy contributions in dictating the composition dependence of  $\gamma$ . For (100)-oriented crystal-melt interfaces the results suggest that roughly only 25% of the temperature dependence is obtained from interface-adsorption contributions, with the remaining due to  $S_{xs}$ . The analysis yields composition-averaged estimates of  $S_{xs}^{(2)}$  in the range of  $-0.45$  to  $-0.6 \sigma_{22}^{-2}$  for the (100) interface. This estimate is considerably larger in magnitude than a previously reported value for pure elements in the Lennard-Jones system.<sup>36</sup>

We end by noting that the current work has only considered adsorption and excess-entropy contributions to  $\gamma$  for (100)-oriented interfaces in face-centered-cubic alloys. Further work is required to determine the anisotropies of these contributions, in order to gain insights into the microscopic origins of the composition dependencies of  $\gamma$  anisotropies. The methods and analysis approaches described in this and our previously published calculations for the present Lennard-Jones system<sup>6,16,40</sup> should be generally applicable in such future studies.

#### ACKNOWLEDGMENTS

This research was supported by the U.S. Department of Energy, Office of Basic Energy Sciences, through Grant No. DE-FG02-06ER46282, and the Computational Materials Science Network. Sandia is a multiprogram laboratory operated by Sandia Corporation, a Lockheed Martin Co., for the DOE's National Nuclear Security Administration under Contract No. DE-AC04-94AL85000. C.A.B. would like to acknowledge the support of the NIST/NRC postdoctoral research associateship program. Portions of this work were performed by C.A.B. and M.A. in the Department of Materials Science and Engineering at Northwestern University and J.J.H. at Sandia National Laboratories. We gratefully acknowledge numerous helpful discussions with Brian Laird.

#### APPENDIX: SENSITIVITY OF CFM RESULTS TO DETAILS OF THE ANALYSIS

In the CFM interfacial free energy calculations, the sources of error can be divided into two categories. The first is associated with finite-sampling, statistical uncertainties in the calculation of  $\langle |A(k)|^2 \rangle$ ; these errors are relatively straightforward to estimate and are routinely reported in published CFM studies. The second category involves errors that are systematic in nature and are associated with the details of (i) the fitting procedure used to extract the stiffness values from the  $\langle |A(k_1, k_2)|^2 \rangle$  data, and (ii) the method used to locate interface positions in the calculation of the Fourier amplitudes  $A(k_1, k_2)$ . In this appendix we summarize the results of tests aimed at assessing the magnitudes of these errors; re-

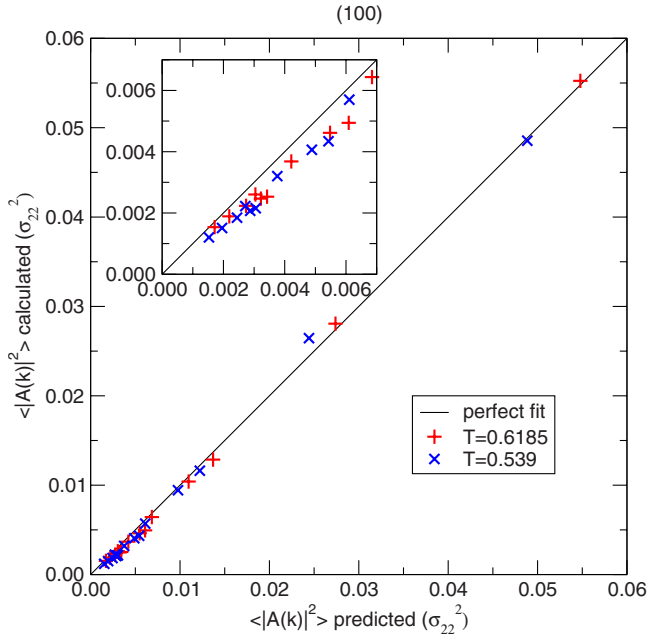


FIG. 9. (Color online) Calculated vs predicted stiffnesses for the (100) orientation of the  $\beta=0.75$ ,  $\alpha=1.0$  system with  $T=0.6185$  and  $T=0.539$   $\epsilon_{22}/k_B$ .

lated analyses of the errors associated with the CFM can also be found in Ref. 23.

Considering first item number (i), Figs. 9 and 10 compare values for  $\langle |A(k)|^2 \rangle$  derived from MD versus those predicted by the least-squares fitting procedure at  $T=0.6185$  (corresponding to pure species 2) and  $T=0.539$  (corresponding to the most concentrated alloy composition considered). The solid line represents perfect agreement between the predicted

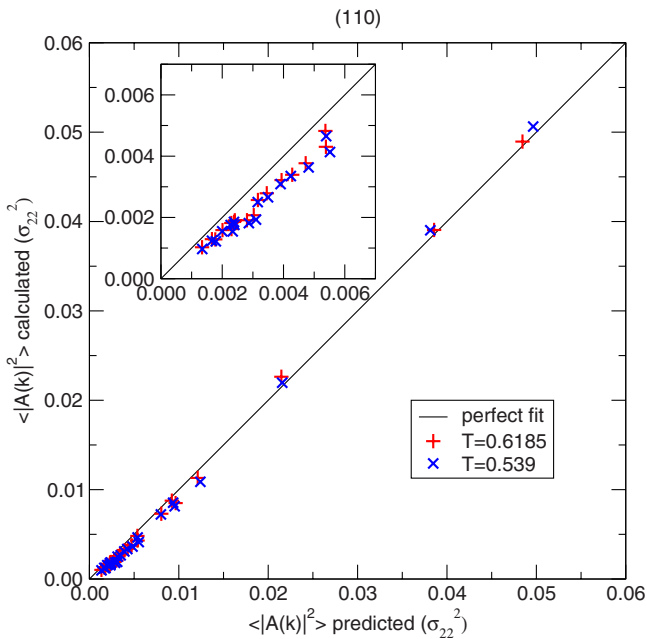


FIG. 10. (Color online) Calculated vs predicted stiffnesses for the (110) orientation of the  $\beta=0.75$ ,  $\alpha=1.0$  system with  $T=0.6185$  and  $T=0.539$   $\epsilon_{22}/k_B$ .

and calculated values. The inset shows the region of low  $\langle |A(k)|^2 \rangle$  values (corresponding to high values of  $k$ ) in greater detail. It is noted that the high- $k$  data is systematically underestimated in the fit. While this is not surprising, given that Eq. (11) is only strictly valid for large fluctuation wavelengths, it does highlight the issue concerning the range of  $k$  over which the data should be fit. One option is to exclude data for values of  $|k|$  beyond a certain cutoff, which can be selected to minimize the reduced  $\chi^2$  values in the least-squares fit.

Alternatively, one can use a modified form of Eqs. (13) and (14) which might be expected to be valid over a larger range of  $k$  values. In particular, the systematic deviation of the high- $k$  data from the  $1/k^2$  fit could in principle arise from higher-order curvature terms. It is known for membranes that the energy of a height fluctuation depends on the wave vector as  $a*k^2 + b*k^4$ , where the second contribution is a “bending rigidity” term.<sup>41</sup> The higher-order  $k^4$  term is also expected to be present for diffuse interfaces when the radius of curvature becomes comparable to the interface width.<sup>42</sup> To estimate whether such higher-order terms could account for the deviations of the high- $k$  data from the  $1/k^2$  fits, we refit the (100) and (110) fluctuation data employing modifications of Eq. (11) adding symmetry-compatible  $k^4$  terms in the denominator.<sup>43</sup> It was found that the resulting values of  $\gamma_0$  were consistently lower, by roughly 5%, than the values given in Table V. This difference was found to be nearly constant for all the temperatures considered, so that the  $T$  dependence of the  $\gamma$  values shown in Fig. 7 remained practically unchanged except for a uniform scaling of the  $\gamma$  results to slightly lower values. For the anisotropy parameters the new fit yielded values that were roughly 10% smaller for  $\epsilon_1$  and as much as 40% larger in magnitude (but with the same negative sign) for  $\epsilon_2$ ; in all cases the differences in the  $\epsilon$  values between the two fits were smaller than the statistical uncertainties for these parameters. Further, the overall trend for the composition dependence of the  $\epsilon$  values reported in Ref. 6 was found from both fits: slight decreases in  $\epsilon_1$  are coupled with a more significant increase in the magnitude of  $\epsilon_2$  as one moves from dilute to concentrated compositions.

We consider next the methods used to identify the interface location. In order to investigate the sensitivity of the calculated stiffnesses to the method used to determine the interface height profile, we performed additional analysis of the snapshots for both the (100) and (110) interfaces for the pure material, and the (100) interface for the alloy at  $T=0.5025$ . The results reported above use the order parameter described in Ref. 19. For the additional analysis, two other order parameters were also used. One was the order parameter from Ref. 21, using time snapshots, rather than the time averaged atomic positions used there. The third order parameter is like the one from Ref. 19, in that it compares the 12 nearest neighbors of each atom with the expected neighbors in the solid phase, but instead of the differences in position it sums the squares of the sines of the angles between the directions to the actual neighbors and the expected neighbors. Smoothed gridding onto a  $10 \times 10$  or  $20 \times 20$  grid instead of the binned  $10 \times 10$  grid used in the results that are reported above, with two choices of the width of the smoothing, were also tried. Not all combinations of these options were con-

sidered, but a total of ten combinations were computed for the alloy, and based on those results, five combinations were computed for the pure material. A number of different fits were performed for each combination: Eq. (11) was used with three different choices for the value of the cutoff of the high- $k$  data excluded from the fit, and the modification to Eq. (11) to include  $k^4$  terms were also employed as described above. For the latter, the fitted coefficients of the  $k^4$  terms were found to vary by up to a factor of 4 depending on the how the shape of the interface is determined. This suggests that all, or at least most, of the apparent  $k^4$  dependence of the  $\langle |A(k_1, k_2)|^2 \rangle$  data at high  $k$  is a nonphysical artifact. The stiffness values, that is the coefficients of the  $k^2$  terms, were found to depend only slightly on how the interface positions

were determined, particularly if the  $k^4$  terms were included in the fit: the stiffnesses showed variations on the order of 5% for the different methods using the  $k^2$  fits, while the variation was smaller, on the order of 1%–2% for the fits including the  $k^4$  terms.

Overall, the results of the analyses summarized in this section suggest that the systematic errors lead to uncertainties in  $\gamma_0$  on the order of 5%, which are about twice as large as the statistical errors reported above. For the  $\epsilon$  parameters, the uncertainties found here are smaller than the corresponding statistical uncertainties. Importantly, the concentration dependencies derived for the  $\gamma_0$  and  $\epsilon$  parameters, which are the primary focus of Ref. 6 and the present paper, are found to be highly robust.

\*cbecker@nist.gov

- <sup>1</sup>W. Kurz and D. J. Fisher, *Fundamentals of Solidification* (Trans Tech, Aedermannsdorf, Switzerland, 1998).
- <sup>2</sup>D. Herlach, D. Holland-Moritz, and P. Galenko, *Metastable Solids from Undercooled Melts* (Elsevier, New York, 2007).
- <sup>3</sup>J. S. Langer, in *Chance and Matter*, edited by J. Souletie, J. Vannimenus, and R. Stora (North-Holland, Amsterdam, 1987).
- <sup>4</sup>W. J. Boettinger, S. R. Coriell, A. L. Greer, A. Karma, W. Kurz, M. Rappaz, and R. Trivedi, *Acta Mater.* **48**, 43 (2000).
- <sup>5</sup>T. Haxhimali, A. Karma, F. Gonzales, and M. Rappaz, *Nature Mater.* **5**, 660 (2006).
- <sup>6</sup>C. A. Becker, D. Olmsted, M. Asta, J. J. Hoyt, and S. M. Foiles, *Phys. Rev. Lett.* **98**, 125701 (2007).
- <sup>7</sup>N. Eustathopoulos, *Int. Met. Rev.* **28**, 189 (1983).
- <sup>8</sup>A. Passerone and N. Eustathopoulos, *Acta Metall.* **30**, 1349 (1982); *J. Cryst. Growth* **49**, 757 (1980).
- <sup>9</sup>H. Gabrisch, L. Kjeldgaard, E. Johnson, and U. Dahmen, *Acta Mater.* **49**, 4259 (2001).
- <sup>10</sup>C. H. P. Lupis, *Chemical Thermodynamics of Materials* (Elsevier, New York, 1983).
- <sup>11</sup>J. Q. Broughton and G. H. Gilmer, *J. Chem. Phys.* **79**, 5095 (1983).
- <sup>12</sup>F. Spaepen, *Acta Metall.* **23**, 729 (1975).
- <sup>13</sup>F. Spaepen and R. B. Meyer, *Scr. Metall.* **10**, 257 (1976).
- <sup>14</sup>B. B. Laird, *J. Chem. Phys.* **115**, 2887 (2001).
- <sup>15</sup>H. Ramalingam, M. Asta, A. van de Walle, and J. J. Hoyt, *Interface Sci.* **10**, 149 (2002).
- <sup>16</sup>C. A. Becker, M. Asta, J. J. Hoyt, and S. M. Foiles, *J. Chem. Phys.* **124**, 164708 (2006).
- <sup>17</sup>R. L. Davidchack and B. B. Laird, *Mol. Phys.* **97**, 883 (1999).
- <sup>18</sup>R. Sibug-Aga and B. B. Laird, *Phys. Rev. B* **66**, 144106 (2002).
- <sup>19</sup>J. J. Hoyt, M. Asta, and A. Karma, *Phys. Rev. Lett.* **86**, 5530 (2001).
- <sup>20</sup>J. J. Hoyt, M. Asta, and A. Karma, *Mater. Sci. Eng., R.* **41**, 121 (2003).
- <sup>21</sup>J. R. Morris, *Phys. Rev. B* **66**, 144104 (2002).
- <sup>22</sup>J. R. Morris and X. Song, *J. Chem. Phys.* **119**, 3920 (2003).
- <sup>23</sup>R. L. Davidchack, J. R. Morris, and B. B. Laird, *J. Chem. Phys.* **125**, 094710 (2006).
- <sup>24</sup>J. S. Rowlinson, *Liquids and Liquid Mixtures* (Butterworth Scientific, London, 1982).
- <sup>25</sup>D. A. Kofke and E. G. Glandt, *Mol. Phys.* **64**, 1105 (1988).
- <sup>26</sup>R. L. Davidchack and B. B. Laird, *J. Chem. Phys.* **108**, 9452 (1998).
- <sup>27</sup>D. Du, H. Zhang, and D. J. Srolovitz, *Acta Mater.* **55**, 467 (2007).
- <sup>28</sup>W. R. Fehlner and S. H. Vosko, *Can. J. Phys.* **54**, 2159 (1976).
- <sup>29</sup>D. Frenkel and B. Smit, *Understanding Molecular Simulation: From Algorithms to Applications* (Academic, San Diego, 2002).
- <sup>30</sup>S. J. Plimpton, *J. Comput. Phys.* **117**, 1 (1995).
- <sup>31</sup>M. Asta, J. J. Hoyt, and A. Karma, *Phys. Rev. B* **66**, 100101(R) (2002).
- <sup>32</sup>J. Q. Broughton and G. H. Gilmer, *J. Chem. Phys.* **84**, 5759 (1986).
- <sup>33</sup>R. L. Davidchack and B. B. Laird, *J. Chem. Phys.* **118**, 7651 (2003).
- <sup>34</sup>Y. Mu and X. Song, *J. Chem. Phys.* **124**, 034712 (2006).
- <sup>35</sup>A. P. Sutton and R. W. Balluffi, *Interfaces in Crystalline Materials* (Clarendon, Oxford, 1995).
- <sup>36</sup>J. Q. Broughton and G. H. Gilmer, *Acta Metall.* **31**, 845 (1983).
- <sup>37</sup>W. A. Curtin, *Phys. Rev. B* **39**, 6775 (1989).
- <sup>38</sup>M. R. Hitchcock and C. K. Hall, *J. Chem. Phys.* **110**, 11433 (1999).
- <sup>39</sup>M. Amini and B. B. Laird, *Phys. Rev. B* **78**, 144112 (2008).
- <sup>40</sup>C. A. Becker, J. J. Hoyt, D. Buta, and M. Asta, *Phys. Rev. E* **75**, 061610 (2007).
- <sup>41</sup>K. R. Mecke, *J. Phys.: Condens. Matter* **13**, 4615 (2001).
- <sup>42</sup>P. A. Kralchevsky, J. C. Eriksson, and S. Ljunggren, *Adv. Colloid Interface Sci.* **48**, 19 (1994).
- <sup>43</sup>C. A. Becker, "From Atoms to Dendrites: The Properties of Alloy Crystal-Melt Interfaces from Atomistic Simulations" (Ph.D. dissertation, Northwestern University, 2006).